

1 **Urban Seismic Site Characterization by Fiber-Optic**
2 **Seismology**

3 **Zack J. Spica^{1,2}, Mathieu Perton³, Eileen R. Martin⁴, Gregory C. Beroza⁵, and**
4 **Biondo Biondi⁵**

5 ¹Earthquake Research Institute, The University of Tokyo, Tokyo, Japan.

6 ²Department of Earth and Environmental Sciences, University of Michigan, Ann Arbor, MI 48109, USA

7 ³CONACYT, Instituto de Geofísica UNAM, Unidad Michoacán, Antigua Carretera a Pátzcuaro 8701, 58190,
8 Morelia, Michoacán, Mexico.

9 ⁴Department of Mathematics, Program in Computational Modeling and Data Analytics, Virginia Tech, Virginia,
10 USA.

11 ⁵Department of Geophysics, 397 Panama Mall, Stanford University, Stanford, California 94305-2215, USA.

Corresponding author: Z. J. Spica, zspica@umich.edu

Abstract

Accurate ground-motion prediction requires detailed site effect assessment, but in urban areas where such assessments are most important, geotechnical surveys are difficult to perform, limiting their availability. Distributed acoustic sensing (DAS) offers an appealing alternative by repurposing existing fiber-optic cables, normally employed for telecommunication, as an array of seismic sensors. We present a proof-of-concept demonstration by using DAS to produce high-resolution maps of the shallow subsurface with the Stanford DAS array, California. We describe new methods to assess H/V spectral ratio – a technique widely used to estimate the natural frequency of the soil – and to extract Rayleigh-wave dispersion curves from ambient seismic field. These measurements are jointly inverted to provide models of shallow seismic velocities and sediment thicknesses above bedrock in central campus. The good agreement with an independent survey validates the methodology and demonstrates the power of DAS for microzonation.

Introduction

Rapid population growth has increased the concentration of people, buildings, and infrastructure in urban areas. Many of these urban centers are developed atop sedimentary basins in earthquake-prone regions, which increases their vulnerability to earthquakes due to the presence of soft sediments that amplify and extend earthquake shaking. Soil conditions are known to have a significant influence on ground motion and damage in earthquakes, as has been well documented in the 1985 Michoacán, Mexico and 1995 Kobe, Japan earthquakes, among many others. As a result, seismic building codes [1] include a soil classification to capture the effects of shallow site response (i.e., resonance frequency) and shear wave velocity (i.e., V_s30) on ground motion.

One of the most widely used techniques to estimate seismic site response involves analyzing the Horizontal to Vertical Spectral Ratio (HVSr) [2] of ambient seismic field recordings. The justification for this method is that larger amplitude shear waves are principally responsible for the ground motion at a site and most of their energy is recorded as horizontal motion. Thus, peaks in the spectral ratio represent frequencies that experience local shear-wave amplification. The diffuse wavefield approach [3] provides a theoretical framework for modeling H/V spectral ratio observations and a means to use them to estimate reliable shallow V_s models [e.g., 4, 5], which are essential for ground motion prediction [e.g., 6]. Because it is

46 straightforward to perform, HVSR has become a cornerstone of seismic microzonia-
47 tion [e.g. 7–9].

48 Even though a typical H/V measurement requires only a few tens of minutes
49 of ambient seismic field recording using a tri-axial seismometer, the potential res-
50 olution of H/V microzonation at the scale of a city is limited by the distribution of
51 available measurements due to two main factors: 1) the money/time available for
52 field campaign and 2) the complex physical, geographical, and legal logistics inher-
53 ent to urban settings. Both of these limitations have prevented urban microzonation
54 with H/V spectral ratio from reaching its full potential.

55 In this paper we present an alternative approach that can overcome these
56 limitations through Distributed Acoustic Sensing (DAS) using underground fiber-
57 optic cable repurposed as a seismometer array with a measurement density on the
58 order of meters. DAS systems rely on coherent optical time-domain reflectometry
59 to measure the amplitude and phase of vibrations along a fiber [10]. DAS is used
60 in the oil and gas industry for vertical seismic profiling [11], microseismic moni-
61 toring [12], and time-lapse seismic surveys [13]. Its recent applications to passive
62 earthquake seismology have demonstrated the consistency between earthquake
63 waveforms recorded by DAS and by conventional seismometers [e.g., 14–17]. DAS
64 response has been shown to be broadband, even when using existing telecommu-
65 nication infrastructure not deployed for seismic monitoring [e.g., 14, 18, 19]. Finally,
66 Yu et al. [19] showed it was possible to compute receiver functions by deconvolv-
67 ing vertical-component velocity seismograms from DAS strain recordings.

68 We demonstrate that H/V spectral ratio measurements can be performed with
69 DAS and that it provides reliable geotechnical information in an urban environment
70 with a density that would be difficult to obtain through a standard microzonation
71 campaign. In addition, we extract Rayleigh wave phase dispersion curves from
72 these measurements using ambient-field interferometry, and jointly invert these two
73 observables to infer simple but reliable velocity models of the shallow subsurface
74 with resolution at depth that should be superior to conventional geotechnical sur-
75 veys. Our approach can be used to extract almost continuous V_s profiles along a
76 fiber cable network and could eventually be repeated through time at little addi-
77 tional cost. We illustrate our method using the Stanford DAS array (Fig. 1), which
78 consists of a fiber cable laying in an air-filled PVC conduit (no clamping or cement-
79 ing) [20]. Our results suggest that if a standard velocimeter (i.e, seismometer) is
80 close to a DAS array, similar analysis could be performed on many existing fiber-
81 optic networks around the world.

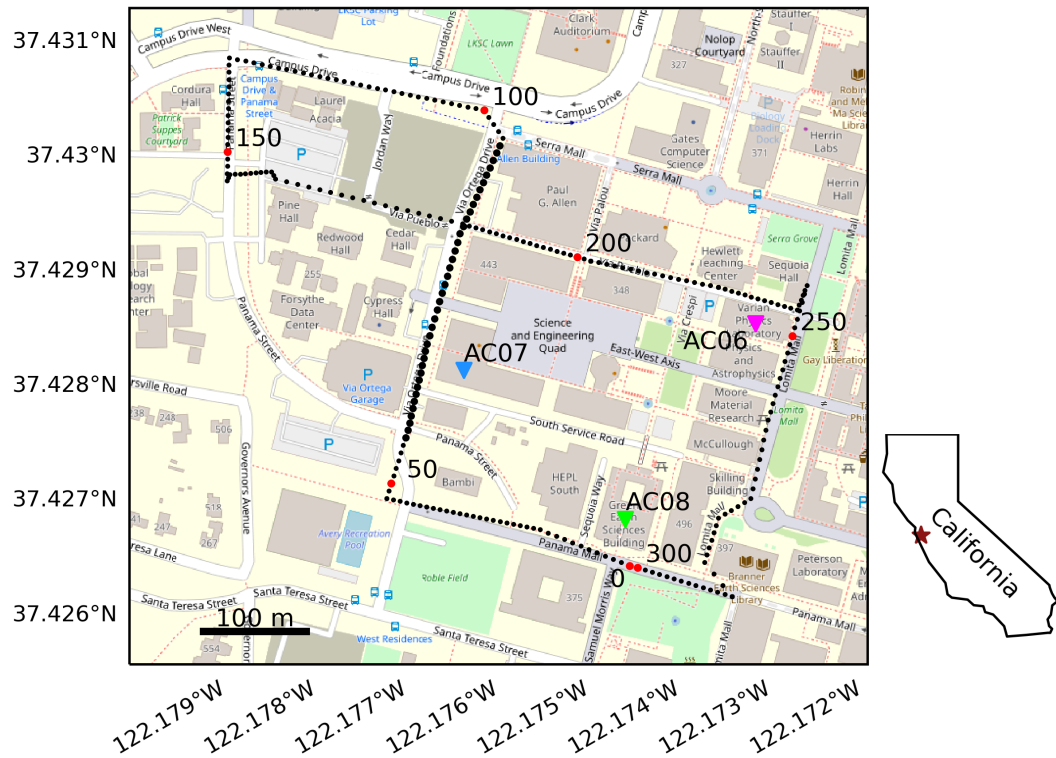


Fig. 1. Map of the Stanford DAS array. Map of the Stanford University campus (West central campus, overlaid on map from Open Street Map) and the fiber-optic array. Each black dot represents the center of a channel along the fiber where a strain measurement is performed. They are spaced at approximately 8 m intervals and numbered from 0 to 300. The multiples of 50 are highlighted with a red dot. Only the 300 (out of 620) first channels are shown as the cable loops twice around its track for overlapping measurements. In this study, we focus on channels 55 to 95 that are located along the Via Ortega Drive and highlighted by thicker black dots. The orange dot depicts the intersection between Via Ortega Drive and Via Pueblo where channels 85 and 185 are orthogonal but co-located. The three inverted triangles depict the velocimeters (i.e., broadband seismometers after removing their instrumental response) used in this study.

82 **Results**

83 **The H/V spectral ratio with DAS**

Based on an extensive theoretical and experimental work, we interpret the H/V spectral ratio as the ratio of the Green's functions, computed through auto-correlation of ambient seismic field [3, 21, 22]. The horizontal energies are computed using the velocity-converted DAS measurement (v_{hor}^{DAS} ; Material and Meth-

ods) and the vertical energies come from a nearby velocimeter ($v_{vert.}^{vel.}$):

$$\frac{H}{V}(\mathbf{x}, \omega) = \sqrt{\frac{2\langle |v_{hori.}^{DAS}(\mathbf{x}, \omega)|^2 \rangle}{\langle |v_{vert.}^{vel.}(\mathbf{x}, \omega)|^2 \rangle}}; \quad (1)$$

84 Computing the H/V spectral ratio with DAS (eq. 1) relies on two major assump-
 85 tions: (i) that a single horizontal component yields a reliable spectral ratio and (ii)
 86 that we can use only one vertical component for a spatially extended distribution of
 87 horizontal components. The reliability of these assumptions is analyzed in the next
 88 two sections through a series of examples in which we compare the Green's func-
 89 tions and their ratios. We refer to the ratios computed with a tri-axial velocimeter
 90 [3] as V-HVSR and to ratios computed by combining DAS and velocimeter mea-
 91 surements as D-HVSR.

92 **A Single Horizontal Component**

93 Fig. 2A shows the displacement Green's function for the 3 components of
 94 velocimeter AC07 and Fig. 2B for the two orthogonal DAS channels (85 and 185)
 95 located at the crossing of the cable along Via Ortega (Fig. 1). The two horizontal
 96 components of the velocimeter share similar characteristics with the two orthogo-
 97 nal components of DAS, which supports assumption (i); however, the DAS mea-
 98 surements (Fig. 2B) undergo fewer spectral oscillations after the main frequency
 99 peak around 1 Hz. Perton et al. [21] and Piña-Flores et al. [23] showed that these
 100 small oscillations are related to the body wave contributions in the Green's func-
 101 tion, while the main peak is related to the Rayleigh contribution. This is because
 102 the velocity-converted DAS Green's function contains a lower proportion of body
 103 waves than the Green's function computed with the velocimeter (Materials and
 104 Methods). We also observe that channel 185 presents a series of high amplitude
 105 spikes, which makes it less suitable for our analysis as it results in a distorted D-
 106 HVSR (Fig. 3A). These spikes could be attributable to different coupling of the ca-
 107 ble at this channel or to transient recording problems.

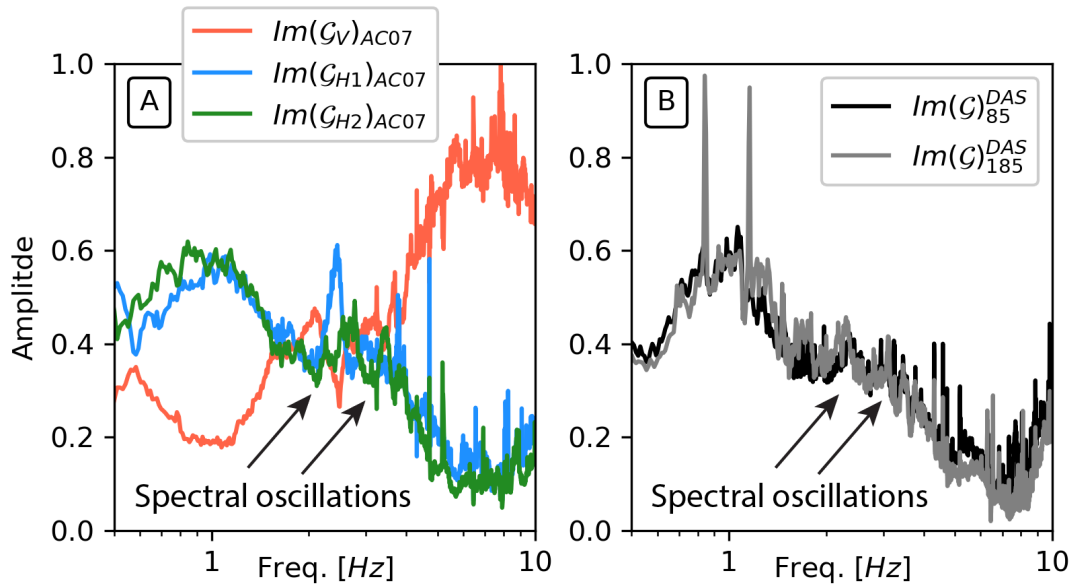


Fig. 2. Single component Green's functions for DAS and velocimeter. (A) $Im(\mathcal{G}_{ii})$ computed from the tri-axial AC07 velocimeter and; (B) computed for the two orthogonal channels 85 and 185.

108 **Ratio of the Green's functions**

109 Fig. 3A compares three different spectral ratios: 1) V-HVSR at station AC07;
 110 2) D-HVSR computed with channel 185 over the vertical component of station
 111 AC07 and; 3) D-HVSR computed with channel 85 over the vertical component of
 112 station AC07. We observe that the overall shape and amplitude of the spectral ra-
 113 tios are very similar. Because the horizontal displacement Green's functions (Fig.
 114 2B) look alike and the vertical displacement Green's function (Fig. 2A) used for
 115 deconvolution is the same, removing the spikes in channel 185 (e.g., with a notch
 116 filter) should lead to a very similar D-HVSR curve. The D-HVSR curves peak at
 117 slightly higher frequency (~ 1.2 Hz) than the V-HVSR (~ 1.0 Hz). Such a difference
 118 is reasonable since along Via Ortega the D-HVSR frequency peaks vary by up
 119 to 0.33 Hz (Fig. 3C). The V-HVSR presents a slightly broader peak than the D-
 120 HVSR. Because the velocimeter and DAS measurements are not co-located, it is
 121 difficult to conclude whether these subtle changes in shape are related to intrinsic
 122 properties of the underlying structure or whether it comes from the measurement.
 123 The good overall agreement of the measurements, however, supports our anal-
 124 ysis and the assumptions behind it. The comparable level of instrumental noise
 125 over 0.1 Hz (Fig. S1) further suggests the measurement is of similar quality. Note

126 that the velocimeters are all located in the basements of buildings about 6 m be-
127 low grade, but on top of thick building foundations, while DAS cable is laying typi-
128 cally 1 m below the surface in a PVC conduit. The thick foundation and the much
129 better coupling of the velocimeter with the ground are likely to provide better low
130 frequency retrieval of the horizontal components that might cause the small dis-
131 crepancy between measurements, although it is also true that observations within
132 buildings are susceptible to cultural noise.

133 In Fig. 3B, we show three different D-HVSR for channel 85, computed with
134 the vertical component of the three different velocimeters present on campus along
135 with the V-HVSR for station AC07. We observe that only the amplitude and not the
136 shape of the D-HVSR curve is affected by the deconvolution of the vertical compo-
137 nent. As expected for such a small scale experiment, the local site conditions are
138 weakly sensitive to the vertical component motion such that it has only a minor ef-
139 fect on the shape of the D-HVSR. In the next analysis, we compute the D-HVSR
140 using the vertical component of velocimeter AC07 because it is closest to the Via
141 Ortega sub-array.

142 We observe small oscillations on both the D-HVSR and V-HVSR around 2.5
143 Hz in figures 3A,B. These oscillations in D-HVSR, suggest that the deconvolution
144 with the vertical component of the velocimeter carries the signature of the body
145 waves. While surface waves propagate in 2-D space and are generally not strongly
146 scattered by lateral heterogeneity, body waves propagate in 3-D space and are re-
147 flected by the free surface and also by strong impedance contrasts at depth. As
148 shown theoretically by Perton et al. [21] for a half space, the waves travelling ver-
149 tically up and down interfere and result in spectral oscillation periods in the energy
150 density components (E_1 , E_2 and E_3 in eq. 5 of the Materials and Methods). They
151 showed that the amplitude of these oscillations in the H/V spectral ratio tends to
152 decay with higher frequencies and that the $H = \sqrt{E_1 + E_2}$ is sensitive to the shear
153 wave velocity while $V = \sqrt{E_3}$ is mainly sensitive to the compressional wave vel-
154 ocity. We clearly observe such a pattern in our measurements, suggesting that the
155 k/ω transformation from strain to particle velocity (Materials and Methods) does
156 not dramatically affect the final shape of the D-HVSR measurements. This is be-
157 cause an important component of the body waves are still present in the vertical
158 component of the velocimeter used for deconvolution of the horizontal DAS compo-
159 nent.

160 Fig. 3C shows all the D-HVSR computed at each channel along Via Ortega
161 along with the V-HVSR for the three velocimeters (colored lines). As highlighted by
162 Ajo-Franklin et al. [17], the local conditions of the fiber can sometimes compromise

163 continuous measurement along the fiber. Fig. 3C shows that except for two chan-
 164 nels (82 and 97), all sensors are able to recover the main frequency peak along
 165 Via Ortega with some variation. The main frequency peaks are highlighted by a
 166 red dot and vary from 1.12 to 1.45 Hz. It appears that the fundamental frequency
 167 of resonance varies smoothly over central campus suggesting a likely homoge-
 168 neous geological structure (at this scale) under the DAS array. For station AC07
 169 and AC06, the main peak is at about 1Hz while AC08 shows a flat V-HVSR curve,
 170 suggesting a lower velocity contrast at depth for this location and for the analyzed
 171 frequency range.

172 The good agreement between V-HVSR and D-HVSR validates the methodol-
 173 ogy and the processing, and provides constraints on potential resonance frequen-
 174 cies at sites across campus.

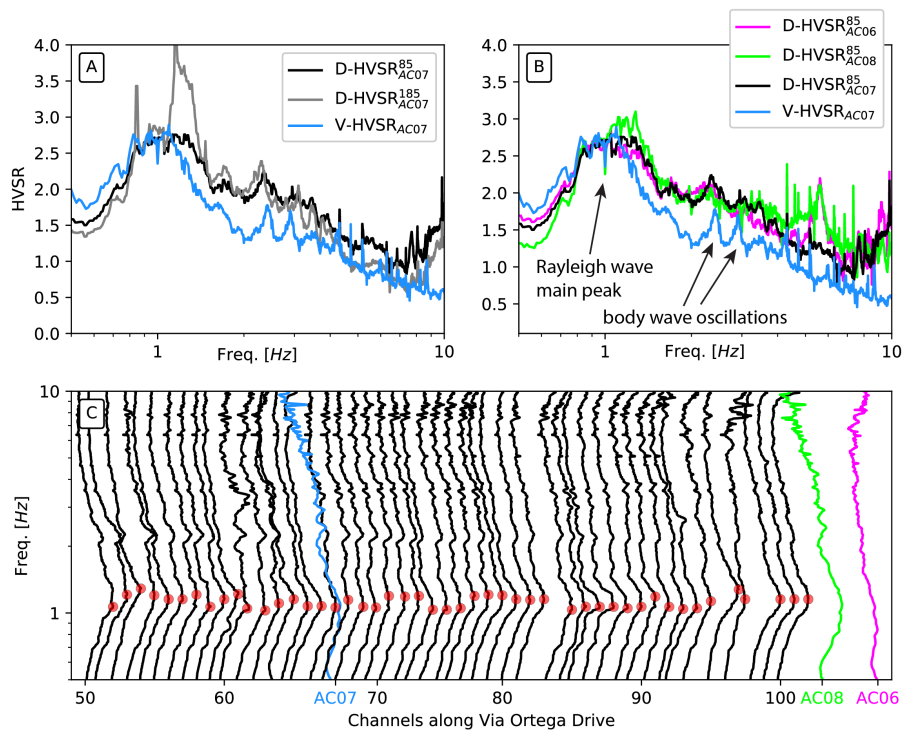


Fig. 3. Comparison between DAS and velocimeter H/V spectral ratios. (A) D-HVSR computed with channel 85 and 185 and V-HVSR for station AC07. (B) Comparison between the V-HVSR at station AC07 and the D-HVSR at channel 85 computed with the vertical component of the three different velocimeters on campus. (C) All the D-HVSR computed along Via Ortega (black) along with the three V-HVSR (color). The frequency of the main D-HVSR peaks are highlighted by a red dot.

175 **Dispersion curves**

176 We calculate Rayleigh-wave phase dispersion images from the monthly virtual-
177 source response estimates (Materials and Methods) via tau-p transforms followed
178 by a Fourier transform in tau. These dispersion images (Fig. 4A) tell us how much
179 energy is traveling at each velocity for a given frequency. For example, at 5 Hz the
180 velocity at channel 85 is 440 m/s, and based on sensitivity analysis such a wave
181 should be sensitive to features in the top ~70 m [24]. These measurements are re-
182 peated for each monthly virtual-source response estimate and based on their vari-
183 ability with time we discard unstable frequencies from further analysis. This vari-
184 ability can be seen when plotting the distribution of picks from monthly dispersion
185 images of multiple virtual source gathers (Fig. 4B). We observe very stable results
186 from ~1.5 Hz up to 8-10 Hz, depending on the virtual source. Because of the lim-
187 ited aperture of the array, dispersion images are unreliable below 1.5-2 Hz.

188 We computed stable dispersion curves every five channels from channel 55
189 to 95. Only nine dispersion curves are computed in order to provide sufficient ar-
190 ray size for dispersion analysis while still allowing for some degree of lateral vari-
191 ation. Each extracted dispersion curve is shown in Fig 4C and compared with a
192 synthetic dispersion curve from an independent velocity model obtained by an in-
193 dependent spectral analysis of surface waves [25] (Fig. S2). The misfit between
194 synthetic and observed velocities is about 50 to 100 m/s. This variation is reason-
195 able given that throughout the Via Ortega fiber, dispersion curves vary by up to
196 100 m/s. Furthermore, in other parts of campus, V_s profiles in the top 100 meters
197 computed by Thomas et al. [25] vary by up to 150 m/s from their local average.

198 **Geotechnical velocity models**

199 We jointly invert the D-HVSR and their co-located dispersion curves to pro-
200 vide shallow velocity models along Via Ortega. An example of the inversion results
201 is shown in Fig. S3 for channel 85. Overall, the agreement for both D-HVSR and
202 the dispersion curve is very good, although below 3 Hz the agreement of the dis-
203 persion curve is slightly worse, indicating some uncertainties with the velocity of
204 the deeper structure. The starting shear wave velocity model obtained by spec-
205 tral analysis of surface waves is shown in magenta in Fig. S3C. Only two layers
206 over a half space were sufficient to fit the observed data. Although simpler, the
207 shallow part of our velocity model agrees well with the initial velocity model. The
208 main frequency peak around 1.2 Hz is well explained with a strong impedance
209 contrast at about 115 m depth. Because the sensitivity of the dispersion curve at

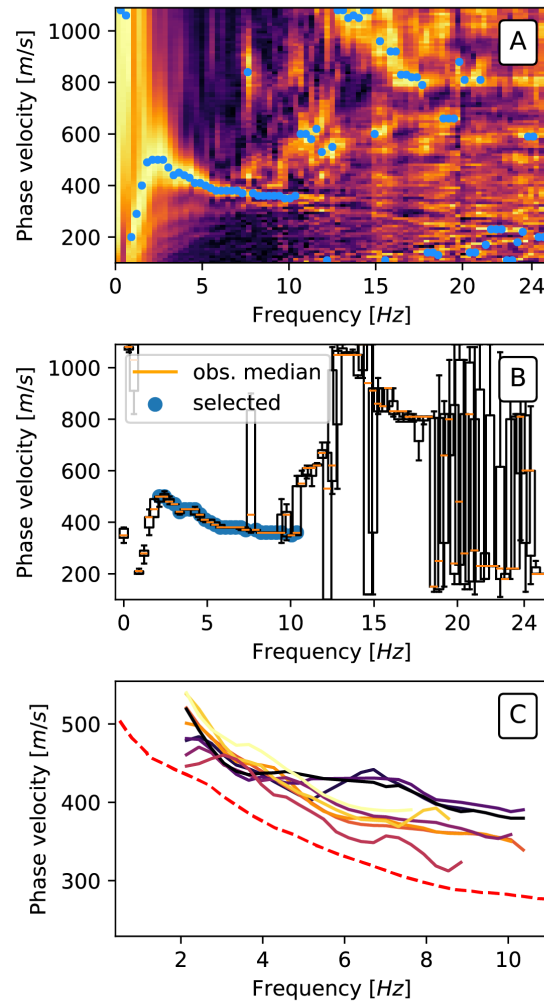


Fig. 4. Dispersion curve analysis. (A) Rayleigh-wave dispersion image for monthly cross-correlations from the channels inline with virtual sources at channel 85. Yellow denotes more energy traveling at a particular frequency and velocity. Dark areas have less energy. The fundamental mode Rayleigh wave is particularly clear. Dots mark local peak velocities. (B) Distribution of each pick's variability versus frequency and velocity. The size of the vertical error bars reflects the variability of the measurement at each frequency. (C) Selected dispersion curves along Via Ortega. The color code refers to their position along Via Ortega. The warmer the color, the farther north along the array is the observed dispersion curve. For comparison, synthetic dispersion curve computed for a velocity model in central campus and shown in Fig. S2 is also shown here in red.

210 such depth is weak, but non-zero, the absolute velocity of the half space is not well
 211 constrained by our observation.

212 Fig. 5 shows all the velocity models computed along Via Ortega. The upper
 213 panel of Fig. 5 also shows an estimate of the V_{S30} for each site. These values are
 214 directly calculated from the joint inversion results. V_{S30} is a widely used indicator of
 215 seismic site conditions and can be easily obtained from our joint inversion method.

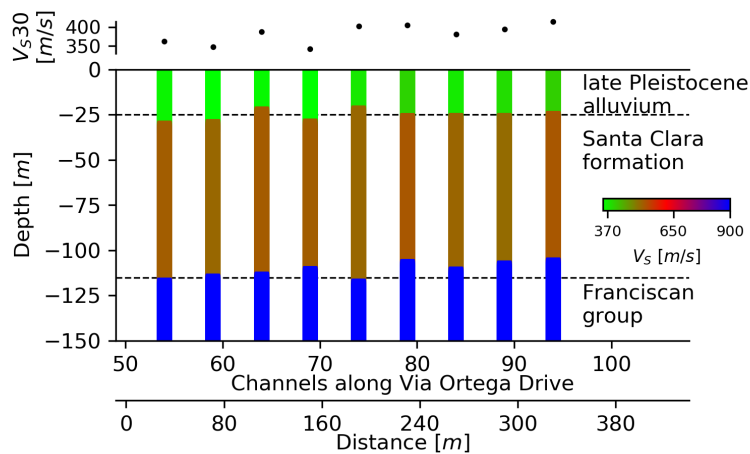


Fig. 5. Joint inversion results and ground truth comparison. The black dashed lines correspond to lithological horizons as described in Thomas et al. [25]. The upper panel shows the V_{S30} estimates extracted from the joint inversion results.

216

217 Discussion

218 Validation with local geology

219 While the values and the lateral variations of the V_{S30} are useful information
 220 for geotechnical engineering, the depth of the basement is also important to char-
 221 acterize the site effect. To validate the reliability of our results, we compare them
 222 to local estimates made as part of an independent geotechnical study on campus
 223 [25] and interpret them in terms of the local lithology.

224 The campus is covered by stiff late Pleistocene alluvial deposits (silty and
 225 sandy clay and dense gravelly silty sand) which vary in thickness from few meters
 226 at the southwest end of the campus to about 40 m at the northeast end [25]. As-
 227 suming it increases linearly between these extremes, the thickness of these de-

228 posits should be 20-25 m under central campus, which is consistent with our ob-
229 servations.

230 These alluvia are underlain by the Santa Clara formation (very stiff to hard
231 clays) to a depth of about 130 m [26, 27]. This formation is well represented by our
232 velocity model although it has a slightly lower thickness. The absolute velocity of
233 this formation ($V_S \sim 500$ m/s) matches well the results obtained by Thomas et al.
234 [25] for central campus (Fig. S3C). In some places the Santa Clara formation is
235 crosscut by the Merced Formation, which mainly consists of poorly consolidated
236 sandstone and claystone. Our models suggests that this formation is either not
237 present, or has no clear seismic expression, under Via Ortega.

238 More controversy exists about the depth of the Franciscan group, which con-
239 stitutes the local basement. Based on the bedrock contour map [28] this crys-
240 talline rock is expected to be approximately ~ 330 m below the surface; however
241 the geotechnical survey suggested it could lie at a much shallower depth (~ 30 to
242 90 m) - at least in the west campus area where a lithological layer with V_S veloc-
243 ity ranging from to 820 to 997 m/s was imaged [25]. Because of the survey de-
244 sign, only one velocity model (of 16) obtained from active source surveys reaches
245 a depth of 100 m. Our velocity models display a strong velocity contrast at about
246 115 m depth. The velocities of the half space obtained from joint inversion of dis-
247 persion curve and D-HVSR agree with velocities of the Franciscan group observed
248 on west campus by Thomas et al. [25]. Knowing the depth of the Franciscan group
249 may significantly reduce uncertainty for site response analysis in central campus.
250 These results suggest that our method allows us to obtain shallow velocity model
251 with a reliability equal or superior to a traditional, dedicated geotechnical survey
252 performed in an urban area.

253 **Relevance to ground motion prediction**

254 For earthquake hazard analysis, engineers are required to estimate the shear
255 wave velocity in the upper 30 m of the subsurface. Knowledge of resonance fre-
256 quencies is also important because they are the frequencies at which soft sedi-
257 ments are expected to amplify ground motion during a seismic event. Finally, the
258 depth to bedrock/basement is also an important parameter for ground motion pre-
259 diction simulations as seismic waves can be trapped by strong impedance con-
260 trasts. All this information in earthquake-threatened cities is generally sparse or
261 nonexistent as it requires expensive and invasive seismic field campaigns. For
262 this reason disaster risk assessment agencies often consider generic models of
263 ground shaking intensity calibrated from observations of past earthquakes world-

264 wide. Here, we demonstrate that existing fiber-optic cable network, otherwise used
265 for communications, can also be used to transform the resolution of microzonation
266 studies in highly populated areas, and that it could do so in a cost-effective way.

267 Compared to previous studies that have discussed the potential of DAS for
268 shallow sub-surface characterization using dispersion curves, our results demon-
269 strated the feasibility of computing H/V spectral ratio measurements from DAS
270 recordings. H/V spectral ratio is an essential component of microzonation studies
271 as it provides both the resonance frequency of a site and after inversion, a veloc-
272 ity model of the subsurface. In this contribution, we inverted dispersion curves and
273 D-HVSR to resolve shallow shear velocities and the depth of the bedrock that con-
274 ventional geotechnical survey failed to image.

275 By providing a local velocity model every 40 m, we offer a description of the
276 shallow geotechnical layer and resonances at the scale of individual buildings. In-
277 creasing this lateral resolution appears to be possible and would open the pathway
278 to analyze new models of ground motion variability. Considering a longer fiber ca-
279 ble offers the possibility of analyzing the variability of site-specific ground motion
280 along distributed infrastructure related to energy, water, or transportation over long
281 distances.

282 **Conclusions and future implications**

283 This study demonstrates the feasibility of H/V spectral ratio using a DAS-
284 recorded ambient seismic field alongside a single velocimeter recording, and il-
285 lustrates the efficacy of such measurements for near-surface imaging in highly
286 populated urban environments. As a low-cost dense array, DAS could be a pow-
287 erful system to assess site effects and the basement depth in other earthquake-
288 threatened areas around the world, including mega-cities such as Mexico City,
289 Tehran, Tokyo, or Djakarta that face extreme earthquake risk.

290 **Materials and Methods**

291 **The Stanford DAS array**

292 DAS uses a standard fiber-optic cable as both an axial strain sensor and a
293 means of transmitting its own data to a storage unit. An interrogator probes the
294 cable via a laser pulse and an interferometer measures the amount of light back-
295 scattered from the heterogeneities (or scatterers) naturally created during the fiber
296 manufacturing process. Such measurement is performed by counting photons
297 within a gauge length and the resulting phase shift is quasi-linearly proportional

298 to the total axial strain change (caused by either axial dilation or compression)
 299 along this section of the fiber [10]. DAS has a lower signal to noise ratio and a
 300 more limited angular sensitivity than standard seismometers; however, this draw-
 301 back is largely compensated by the benefits of having an ultra-dense series of per-
 302 manently installed and highly resistant seismic sensors communicating over large
 303 distances and running on a single power source [29].

304 The Stanford DAS array was created using a fiber cable loosely deployed in
 305 an air-filled PVC conduit (~12 cm wide) managed by Stanford IT Services (Fig. 1).
 306 The coupling between the cable and the surrounding rock relies therefore exclu-
 307 sively on gravity and friction. The Stanford DAS array recorded and stored contin-
 308 uous data from 620 independent seismic channels at a frequency of 50 samples
 309 per second with 7.14m gauge length and 8.16 m channel spacing. Through this
 310 experiment Martin et al. [20] showed that DAS technology can be used to record
 311 seismic data directly from a free-floating cable in a horizontal PVC conduit. Fur-
 312 thermore, by analyzing adjacent earthquakes on nearby faults, Biondi et al. [14]
 313 demonstrated that signals recorded using this cable provide repeatable and reliable
 314 ground motion measurements. More details about the array design, geometry and
 315 setup can be found in Biondi et al. [14] or Martin et al. [30].

316 Two different interrogator units were installed at Stanford: OptaSense ODH-
 317 3 and ODH-4. ODH-3 started recording signals in early September 2016 and was
 318 used to compute year-long dispersion curves. ODH-4 only recorded a few days of
 319 seismic data between 2017-10-05 and 2017-10-13. This data was acquired along
 320 with ODH-3 and three broadband velocimeters temporarily installed near the ar-
 321 ray [31]. As ODH-4 recordings show a higher data quality (Fig. S1), it was used to
 322 compute D-HVSR.

323 **From strainmeter to virtual velocimeter**

324 The strain component measured at a channel is the spatial derivative of the
 325 displacement along the cable denoted locally as the direction e_x : $\varepsilon_{xx} = u_{x,x}$. Using
 326 a plane wave decomposition $\mathbf{u}(\mathbf{x}, t) = \mathbf{U}e^{i(\mathbf{k}\mathbf{x} - \omega t)}$, we can express the strain compo-
 327 nent as $\varepsilon_{xx} = -ik_x u_x$; where \mathbf{k} , ω , i and \mathbf{x} are the wave number vector, the angular
 328 frequency, the imaginary number, and the position, respectively. Since the particle
 329 velocity is the time derivative of the displacement ($v_x = \dot{u}_x = \frac{du_x}{dt} = -i\omega u_x$), we ob-
 330 tain the relationship linking strain to particle velocity as: $\varepsilon_{xx} = -ik_x u_x = \frac{k_x}{\omega} \dot{u}_x$; and
 331 as the modes propagate along the surface in the direction e_x with a phase velocity

332 given by $c = \frac{\omega}{k_x(\omega)}$, previous studies [e.g., 16, 19] used:

$$\varepsilon_{xx} = \frac{1}{c} v_x \quad (2)$$

333 to compare DAS strain to velocimeter records.

334 In eq. 2, k_x depends on ω according to the different modes, and depends on
 335 both the subsurface velocity structure and the wavefront's angle of incidence. As
 336 the fundamental Rayleigh wave mode always has the highest k_x for any frequency
 337 (ignoring Love waves), it is strongly amplified by the DAS measurement. The lat-
 338 ter is illustrated by the theoretical $\omega - k_x$ diagrams for both strain and velocity (Fig.
 339 S4) in which we observe that the first Rayleigh mode dominates the strain spec-
 340 trum. Fig. S4 is obtained using a V_S velocity model for central campus (Fig. S2)
 341 previously produced by an independent study based on spectral analysis of sur-
 342 face waves [25]. The calculation was performed using the Discrete Wave Number
 343 method [32]. The bright colors in the figure correspond to higher amplitudes.

344 The phase velocity c modulates the seismogram recorded by DAS and has
 345 a major effect on the amplitude. Because c varies generally smoothly, its effect on
 346 the phase of the signal is muted; which explains the success of previous travel-
 347 time based analyses, using both local and teleseismic earthquakes or ambient
 348 seismic field directly with DAS strain recordings[19, 33]. Because body waves have
 349 almost no dispersion, DAS measurements allows measurement of their travel-times
 350 directly from strain records [34].

351 Eq. 2 can be used to retrieve the phase velocity of the fundamental Rayleigh
 352 wave (c_{R_0}) if both v_x (from a velocimeter) and ε_{xx} (from DAS) measurements are
 353 available at a site [e.g., 19]. The particle velocity of the fundamental Rayleigh mode
 354 is calculated by applying the transformation $v_x = c_{R_0} \varepsilon_{xx}$ to DAS measurements
 355 [16, 19]; however, by doing so, it is important to keep in mind that we artificially en-
 356 hance the contribution of the Rayleigh mode compared to amplitudes measured by
 357 a traditional velocity sensor. Other factors such as the gauge length, the angle of
 358 incidence of the wavefield, and the coupling of the fiber with the ground may also
 359 influence the amplitude.

360 We can compare DAS and velocimeter measurements (Fig. S5) by convert-
 361 ing strain to particle velocity using a theoretical Rayleigh phase dispersion curve
 362 obtained from the velocity model showed in Fig. S2. This comparison is conducted
 363 for both ambient seismic field and earthquake waveforms in both time and spectral
 364 domains with reference to velocimeter AC07. The ambient seismic field is recorded
 365 at one of the closest channels to station AC07 (channel 70, which is ~30 m dis-

366 tant) while the earthquake (2017-10-08 01:40:15, Md 2.8, 36.847°N 121.577°W,
 367 next to Hollister, CA) is recorded at channel 185 with orientation closer to the wave
 368 propagation direction. Channel 185 is located on Via Ortega Drive but is orthog-
 369 onal to the direction of the road (parallel to Via Pueblo; orange dot in Fig. 1). To
 370 facilitate the comparison, waveforms of the horizontal components of the station
 371 AC07 were corrected for instrument response and rotated according to the fiber
 372 orientation. DAS clearly records the ambient seismic field and earthquake wave-
 373 forms with comparable phase and amplitude to the seismometer. Although the
 374 signal to noise ratio of DAS is lower than conventional broadband sensors, small
 375 transient signals (i.e., nearby vehicles) of small amplitude can be recorded with a
 376 single channel, as observed around 30 s time lag in Fig. S5A.

377 **Computing the H/V spectral ratio with DAS**

378 In its simplest form, the H/V spectral ratio is the square root of the ratio of the
 379 spectral energy components of a tri-axial ground-motion sensor [35]:

$$\frac{H}{V}(\mathbf{x}, \omega) = \sqrt{\frac{E_1(\mathbf{x}, \omega) + E_2(\mathbf{x}, \omega)}{E_3(\mathbf{x}, \omega)}}; \quad (3)$$

380 where indices 1 and 2 stand for the horizontal components, index 3 stands for the
 381 vertical component and ω is the angular frequency. Under a diffuse field assump-
 382 tion, Pertou et al. [21] showed that the spectral energy ($E_i(\mathbf{x}, \omega)$) can be computed
 383 from the average auto-correlation of the wavefield components and is proportional
 384 to the imaginary parts of the Green's function:

$$E_i(\mathbf{x}, \omega) = \langle v_i(\mathbf{x}, \omega)v_i^*(\mathbf{x}, \omega) \rangle \propto -\omega \text{Im}[\mathcal{G}_{ii}(\mathbf{x}, \mathbf{x}, \omega)]; \quad (4)$$

385 where $v_i(\mathbf{x}, \omega)$ is the velocity field in direction i at a point \mathbf{x} , the $*$ denotes the com-
 386 plex conjugate operator and the brackets $\langle \cdot \rangle$ denote averaging over time. In the fre-
 387 quency domain, the product $v_i(\mathbf{x}, \omega)v_i^*(\mathbf{x}, \omega)$ equals the auto-correlation in the time
 388 domain. In the last term of eq. 4, $\text{Im}[\cdot]$ indicates the imaginary part and $\mathcal{G}_{ii}(\mathbf{x}, \mathbf{x}, \omega)$
 389 is the displacement Green's function due to the application of a unit point force in
 390 the direction i at a location \mathbf{x} . This equation (eq. 4) is the same used for classic
 391 ambient seismic field correlations [36], but for the special case where the source
 392 and receiver are co-located.

Within this framework, Sánchez-Sesma et al. [3] proposed a theoretical de-
 scription of the H/V spectral ratio and suggested that it could be directly computed

in terms of the ratio of the imaginary part of the Green's functions as:

$$\frac{H}{V}(\mathbf{x}, \omega) = \sqrt{\frac{\text{Im}[\mathcal{G}_{11}(\mathbf{x}, \mathbf{x}, \omega) + \mathcal{G}_{22}(\mathbf{x}, \mathbf{x}, \omega)]}{\text{Im}[\mathcal{G}_{33}(\mathbf{x}, \mathbf{x}, \omega)]}}. \quad (5)$$

DAS measurements only describe the component of motion along the fiber, which prevents the use of eq. 3; however, under the diffuse field assumption, and in the absence of strong horizontal heterogeneity or lateral anisotropy, the horizontal spectral energies should be equal regardless of their orientation [21]. Therefore, eq. 5 can be simplified as:

$$\frac{H}{V}(\mathbf{x}, \omega) = \sqrt{\frac{2\text{Im}(\mathcal{G}_{11}(\mathbf{x}, \mathbf{x}, \omega))}{\text{Im}(\mathcal{G}_{33}(\mathbf{x}, \mathbf{x}, \omega))}}; \quad (6)$$

393 where the horizontal DAS measurement is used for the numerator. Because the
 394 vertical component of motion is expected to be relatively insensitive to the local
 395 site conditions [e.g., 19, 37], especially for a spatially limited region, the vertical
 396 component of a nearby velocimeter is used as the denominator in eq. 6. If both
 397 DAS and velocimeter recordings share same units (i.e., after conversion to veloc-
 398 ity) the D-HVSR can be computed as in eq. 1. These set of equations are only
 399 valid when the seismic wave field is equipartitioned, that is, all the incident waves
 400 have the same energies [38]. As this assumption is unlikely to be true, the equipar-
 401 titioning of the seismic wavefield must be enhanced through signal processing, just
 402 as for traditional ambient seismic field cross-correlation [39].

403 **Computing the Green's functions**

404 As in Spica et al. [22], we first remove the contribution of non-stationary sources
 405 such as transients and small earthquakes by applying a running absolute mean
 406 normalization in the time domain. We then apply spectral whitening, which cor-
 407 responds to source deconvolution. Because several sources can act in different
 408 frequency bands and with different energy for the horizontal or the vertical com-
 409 ponent (Fig. S4), the operation consists of normalizing the signals by the source
 410 energies computed in each time window and across several frequency bands. It
 411 is computed as: $\tilde{v}_i(\mathbf{x}, \omega) = v_i(\mathbf{x}, \omega) / \sqrt{2|v_{hor.}^{DAS}(\mathbf{x}, \Delta\omega)|^2 + |v_{vert.}^{velo.}(\mathbf{x}, \Delta\omega)|^2}$; where $\Delta\omega$
 412 is a frequency band of 0.7 Hz width centered on ω . Here, the particle velocity is
 413 taken in each time window as $v_x(\omega) = c_{R_0}(\omega)\varepsilon_{xx}(\omega)$ with $c_{R_0}(\omega)$ being the reference
 414 dispersion curve for central campus. To remove only the spectral envelope, the
 415 bandwidth has to be much larger than the oscillations in the spectra (Fig. 2) and
 416 because the DAS and velocimeter channels are not co-located, the time window

417 should be large enough to allow the effect of sources to pass across the array.
418 In this experiment the time window was set to 20s with an overlap of 80%. Both
419 the running absolute mean normalization and the whitening tends to equalize the
420 spectral energies and enhance the equipartitioning. It is an essential component of
421 the data processing that also tends to reduce the gap in sensitivity between DAS
422 and velocimeter measurements. In that sense, the processing we apply to the data
423 is substantially different than other studies that compute H/V spectral ratio following
424 Nakamura [2].

425 **Rayleigh-wave interferometry**

426 We apply passive Rayleigh-wave interferometry to the DAS channels along
427 Via Ortega using one year of continuous data starting from early September 2016
428 [20]. Only a collinear sub-array is used for interferometry because that virtual source
429 configuration is expected to yield Rayleigh waves [29]. We apply cross-correlation
430 of ambient seismic field with minimal preprocessing. We window of continuous sig-
431 nal into five minute intervals with 50% overlap, band-passed filter from 0.5-24 Hz,
432 perform a 1-bit normalization, and then stack hourly cross-correlations. After sav-
433 ing each hour's average cross-correlations throughout the week, we normalized
434 them by their L1 norms and stack them for each month, yielding a series of virtual-
435 source response estimates Martin et al. [20].

436 **Joint inversion and shallow V_S estimates**

437 In eq. 5, the $\text{Im}(\mathcal{G}_{ii})$ components are associated with the shallow local struc-
438 ture, which we approximate locally with a horizontally layered geometry having ma-
439 terial properties (V_S) that vary only with depth; however, the fundamental mode of
440 the Rayleigh wave dominates the ambient seismic field (Fig. S4), the direct prob-
441 lem used to compute the $\text{Im}(\mathcal{G}_{ii})$ should account this. Among the several methods
442 that exist to compute these $\text{Im}(\mathcal{G}_{ii})$ under a diffuse field assumption [e.g., 5, 32,
443 38, 40], we use the analytical representation proposed by García-Jerez et al. [40]
444 because it allows us to modulate the contributions of the various waves. For ex-
445 ample, we are able to compute the $\text{Im}(\mathcal{G}_{ii})$ considering only the first higher mode
446 Rayleigh wave (no Love waves) along with body waves.

447 It is well known that consideration of H/V solely at the surface is insufficient to
448 characterize shallow properties uniquely due a trade-off between layer velocity and
449 thickness that leads to a similar H/V curves [23, 41]. Additionally, the forward prob-
450 lem is highly non-linear and depends on several uncorrelated parameters [23, 40].

451 We therefore better constrain the inversion by inverting jointly the phase dispersion
452 curve and the D-HVSR observations using an existing V_S velocity model from cen-
453 tral campus (Fig. S2) as the starting model for the inversion. While the H/V spec-
454 tral ratio is mainly sensitive to sharp impedance contrasts and vertical travel time, it
455 has poor sensitivity to the absolute value of the velocities. On the other hand, dis-
456 persion curves are only weakly sensitive to the depth of structural variations due to
457 the broad sensitivity kernels of surface waves with depth, but they are highly sen-
458 sitive to the absolute velocity of the medium. The complementary nature of these
459 measurements makes it a powerful combination for subsurface characterization
460 [22]. Details of the inversion scheme can be found in Piña-Flores et al. [23].

461 **Acknowledgments:** The Stanford fiber-optic array and data acquisition was
462 made possible by a collective effort from Stanford IT services, Stanford Geophysics
463 and OptaSense Ltd. In particular we would like to thanks Martin Karrenbach, Steve
464 Cole, Chris Castillo, Ethan Williams, Siyuan Yuan, Gregory Kersey, Paul Narcisse,
465 and Gary Gutfeld for their efforts in deploying, calibrating, or operating the DAS
466 instruments. We thank OptaSense for donating the interrogator unit for the array
467 in Stanford. We thank USGS for deploying the velocimeters. We thank José Piña-
468 Flores for useful discussion and for providing guidance with the code HVInv. All the
469 figures have been plotted with Matplotlib, and most of the data processing steps
470 have been performed using ObsPy and Pyrocko. The Stanford Center for Compu-
471 tational Earth and Environmental Science (CEES) provided computing resources.
472 **Funding:** B.B. and E.M. thank the Stanford Exploration Project affiliate members
473 for financial support. Eileen Martin was supported by: DOE CSGF under grant
474 DE-FG02-97ER25308, Schlumberger Innovation Fellowship, and the SEP affili-
475 ate companies. **Author contributions:** Z.S. and M.P. discussed and developed
476 the algorithms to compute H/V spectral ratio with DAS. E.M computed the disper-
477 sion curves. Z.S jointly inverted the results to obtain shallow velocity models. B.B
478 and E.M. designed the Stanford DAS array and acquired the data. All authors ac-
479 tively participated in discussing and writing the manuscript. **Competing interests:**
480 The authors declare that they have no competing interests. **Data and materials**
481 **availability:** The DAS data used in this study was acquired by OptaSense and
482 can be shared upon request to B.B. The data from the broadband seismometers
483 can be accessed at <http://ds.iris.edu/gmap/#network=GM&planet=earth> (last

484 access June 2019). Code for joint inversion is accessible at <https://w3.ual.es/>
485 GruposInv/hv-inv/ (last access June 2019).

Supplementary Materials:

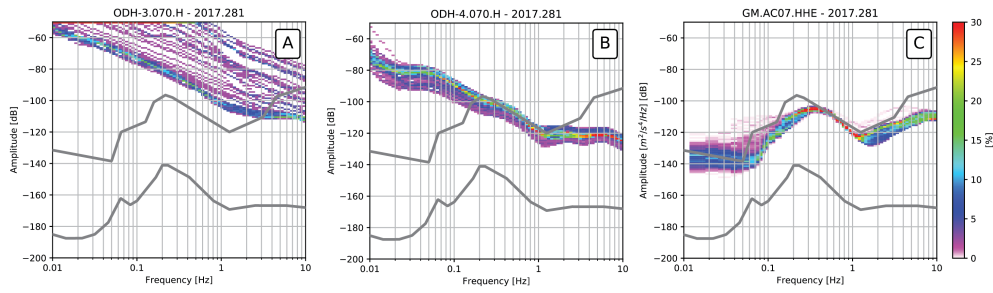


Fig. S 1. Power spectral densities Power spectral density (PSD) function analysis for different recording instruments at Stanford. PSD were computed following [42] and for each instrument after conversion of their records to particle velocity. ODH-3 interrogator unit (A) shows a much more unstable pattern of records and much noisier than new generation of sensor ODH-4 (B). Due to the vicinity to the coast, the PSD of ground motion at the microseismic peak is expected to be high, as is observed using the records of the broadband seismometer AC07 (C). Black lines are the high-noise and low-noise model of Peterson et al. [43].

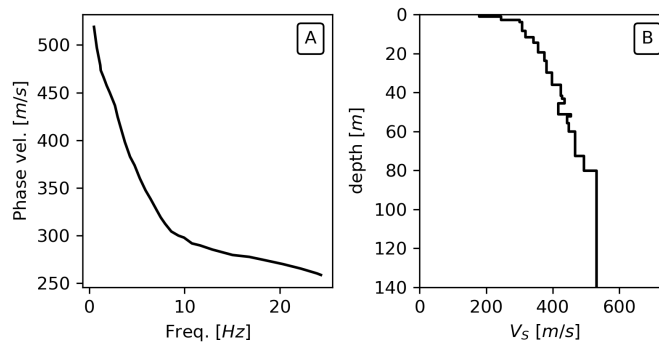


Fig. S 2. Synthetic dispersion curve and starting velocity model. (A) synthetic dispersion curve obtained from velocity model in (B). (B) Average velocity model obtained from spectral analysis of surface waves by Thomas et al. [25]. The lower half-space is extrapolated with constant velocity.

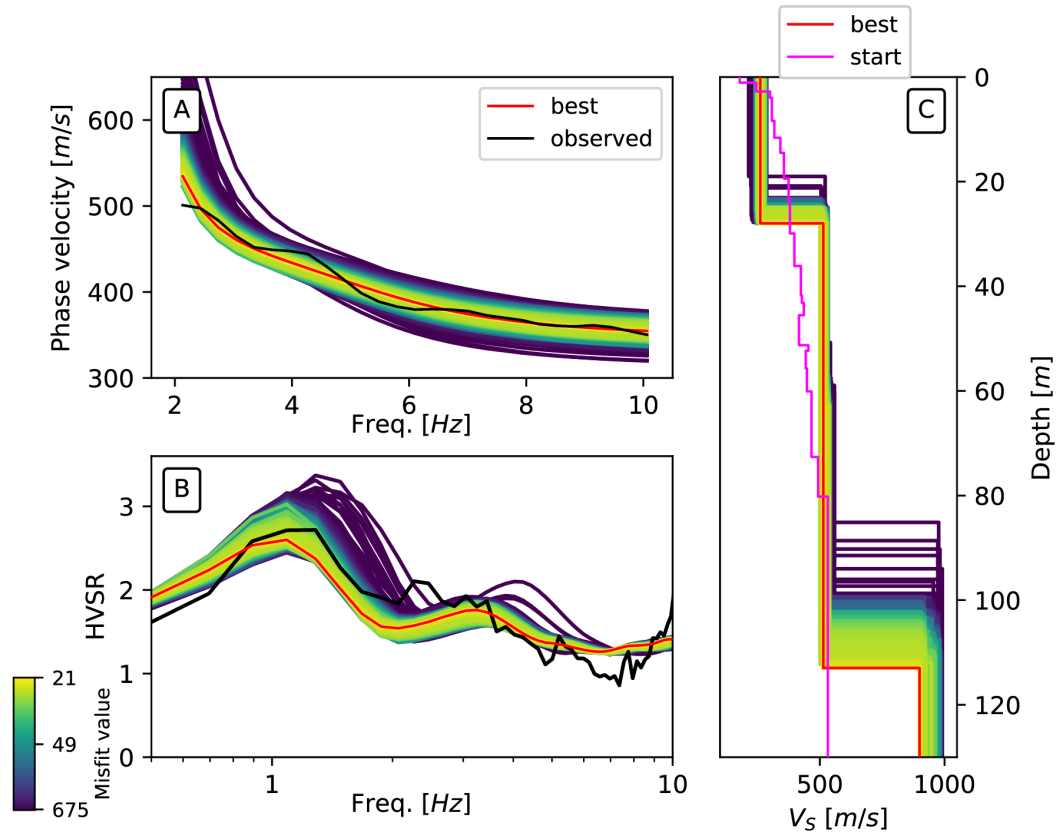


Fig. S 3. Joint inversion result for channel 85. (A) Dispersion curves. (B) D-HVSR. (C) V_S profile. Starting velocity model is shown in magenta. In all panels, lighter colors (i.e., yellow) is associated with a lower misfit value.

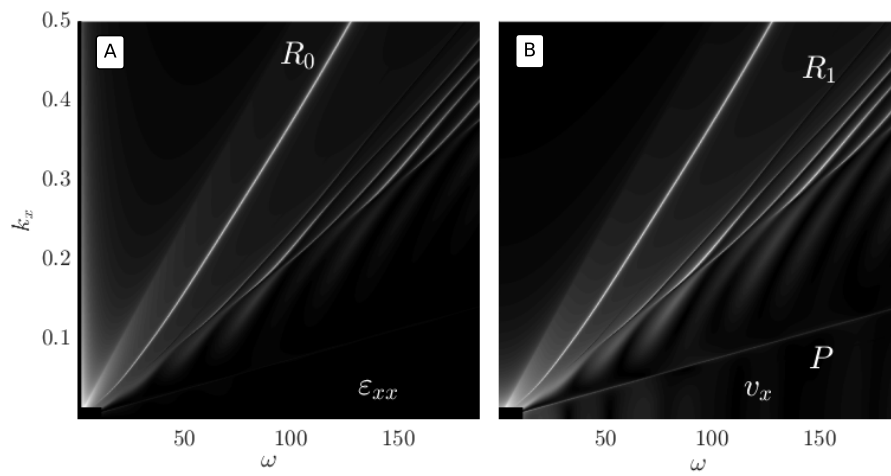


Fig. S 4. $\omega - k_x$ diagrams for strain and velocity. (A) strain $\omega - k_x$ diagram. (B) velocity $\omega - k_x$ diagram. Both diagrams are obtained by simulating the wave propagation with the Discrete Wave Number method using velocity model shown in Fig. 2. The color scale is logarithmic and light colors correspond to higher energies. R_0 and R_1 indicate the fundamental and first higher mode of the Rayleigh wave, respectively. P is the P -wave.

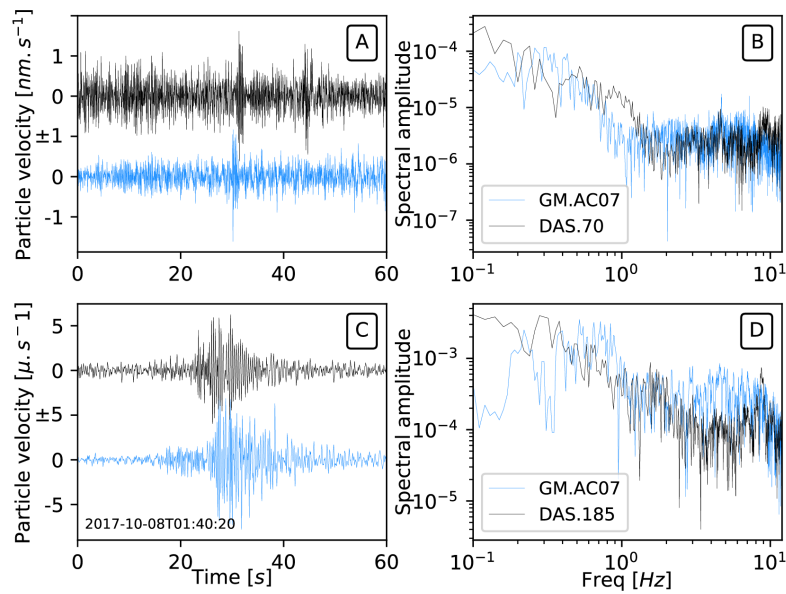


Fig. S 5. Velocity-converted waveforms. Velocity-converted waveforms from DAS (black) and station AC07 (blue). DAS waveforms are converted from strain to velocity using eq. 2 and the geophone waveforms are corrected for instrument response and rotated according to the orientation of the DAS measurement. (A) 60 seconds of ambient seismic field recording (with DAS channel 70), bandpass filtered between 0.8 and 8 Hz. (B) Amplitude spectra of the unfiltered waveforms shown in A. (C) M_d 2.8 earthquake (recorded with DAS channel 185), bandpass filtered between 0.8 and 8 Hz. (D) Amplitude spectra of the unfiltered waveforms shown in C. The velocity waveforms computed from strain are comparable in amplitude and shape to those of the velocimeter station.

487 **References**

- 488 [1] Federal Emergency Management Agency. *NEHRP recommended provisions*
489 *for seismic regulations for new buildings and other structures*. Fema, 2003.
- 490 [2] Y. Nakamura. A method for dynamic characteristics estimation of subsurface
491 using microtremor on the ground surface (in japanese with english abstract).
492 *Railway Technical Research Institute, Quarterly Reports*, 30(1), January 1989.
493 ISSN 0033-9008.
- 494 [3] Francisco J. Sánchez-Sesma, Miguel Rodríguez, Ursula Iturrarán-Viveros,
495 Francisco Luzón, Michel Campillo, Ludovic Margerin, Antonio García-Jerez,
496 Martha Suarez, Miguel A. Santoyo, and Alejandro Rodríguez-Castellanos. A
497 theory for microtremor H/V spectral ratio: application for a layered medium.
498 *Geophysical Journal International*, 186(1):221–225, 2011. ISSN 1365-246X.
499 doi: 10.1111/j.1365-246X.2011.05064.x.
- 500 [4] Zack Spica, Corentin Caudron, Mathieu Perton, Thomas Lecocq, Thierry
501 Camelbeeck, Denis Legrand, José Piña-Flores, Arturo Iglesias, and
502 Devy Kamil Syahbana. Velocity models and site effects at Kawah Ijen vol-
503 cano and Ijen caldera (Indonesia) determined from ambient noise cross-
504 correlations and directional energy density spectral ratios. *Journal of Volcanol-*
505 *ogy and Geothermal Research*, 302:173–189, 2015. doi: 10.1016/j.jvolgeores.
506 2015.06.016.
- 507 [5] M Perton, Z Spica, and C Caudron. Inversion of the horizontal to vertical
508 spectral ratio in presence of strong lateral heterogeneity. *Geophysical Jour-*
509 *nal International*, 2017.
- 510 [6] Julian J Bommer, Peter J Stafford, Benjamin Edwards, Bernard Dost, Ewoud
511 van Dedem, Adrian Rodriguez-Marek, Pauline Kruiver, Jan van Elk, Dirk
512 Doornhof, and Michail Ntinalexis. Framework for a ground-motion model
513 for induced seismic hazard and risk analysis in the Groningen gas field, the
514 Netherlands. *Earthquake Spectra*, 33(2), 2017. doi: 10.1193/082916EQS138M.
- 515 [7] Pierre-Yves Bard. Microtremor measurements: a tool for site effect estimation.
516 In *Proceeding of the Second International Symposium on the Effects of Sur-*
517 *face Geology on Seismic Motion*, volume 3, pages 1251–1279. AA Balkema
518 Rotterdam, 1998.
- 519 [8] Davor Stanko, Snježana Markušić, Stjepan Strelec, and Mario Gazdek. HVSR
520 analysis of seismic site effects and soil-structure resonance in Varaždin city
521 (North Croatia). *Soil Dynamics and Earthquake Engineering*, 92:666–677,
522 2017.

- 523 [9] Zorigt Tumurbaatar, Hiroyuki Miura, and Tsoggerel Tsamba. Site effect as-
524 sessment in Ulaanbaatar, Mongolia through inversion analysis of microtremor
525 H/V spectral ratios. *Geosciences*, 9(5):228, 2019.
- 526 [10] KTV Grattan and T Sun. Fiber optic sensor technology: an overview. *Sensors*
527 *and Actuators A: Physical*, 82(1-3):40–61, 2000.
- 528 [11] A Mateeva, J Mestayer, B Cox, D Kiyashchenko, P Wills, J Lopez, S Grandi,
529 K Hornman, P Lumens, A Franzen, et al. Advances in distributed acoustic
530 sensing (DAS) for VSP. In *SEG Technical Program Expanded Abstracts 2012*,
531 pages 1–5. Society of Exploration Geophysicists, 2012.
- 532 [12] P Webster, J Wall, C Perkins, and M Molenaar. Micro-seismic detection using
533 distributed acoustic sensing. In *SEG Technical Program Expanded Abstracts*
534 *2013*, pages 2459–2463. Society of Exploration Geophysicists, 2013.
- 535 [13] Thomas M Daley, Barry M Freifeld, Jonathan Ajo-Franklin, Shan Dou, Ro-
536 man Pevzner, Valeriya Shulakova, Sudhendu Kashikar, Douglas E Miller, Julia
537 Goetz, Jan Henninges, et al. Field testing of fiber-optic distributed acoustic
538 sensing (DAS) for subsurface seismic monitoring. *The Leading Edge*, 32(6):
539 699–706, 2013.
- 540 [14] Biondo Biondi, Eileen Martin, Stephen Cole, Martin Karrenbach, and
541 Nathaniel Lindsey. Earthquakes analysis using data recorded by the Stan-
542 ford DAS Array. In *SEG Technical Program Expanded Abstracts 2017*, pages
543 2752–2756. Society of Exploration Geophysicists, 2017.
- 544 [15] Nathaniel J Lindsey, Eileen R Martin, Douglas S Dreger, Barry Freifeld,
545 Stephen Cole, Stephanie R James, Biondo L Biondi, and Jonathan B Ajo-
546 Franklin. Fiber-optic network observations of earthquake wavefields. *Geo-*
547 *physical Research Letters*, 44(23):11–792, 2017.
- 548 [16] Herbert F Wang, Xiangfang Zeng, Douglas E Miller, Dante Fratta, Kurt L
549 Feigl, Clifford H Thurber, and Robert J Mellors. Ground motion response to
550 an ml 4.3 earthquake using co-located distributed acoustic sensing and seis-
551 mometer arrays. *Geophysical Journal International*, 213(3):2020–2036, 2018.
- 552 [17] Jonathan B Ajo-Franklin, Shan Dou, Nathaniel J Lindsey, Inder Monga, Chris
553 Tracy, Michelle Robertson, Veronica Rodriguez Tribaldos, Craig Ulrich, Barry
554 Freifeld, Thomas Daley, et al. Distributed acoustic sensing using dark fiber for
555 near-surface characterization and broadband seismic event detection. *Scien-*
556 *tific reports*, 9(1):1328, 2019.
- 557 [18] Philippe Jousset, Thomas Reinsch, Trond Ryberg, Hanna Blanck, Andy
558 Clarke, Rufat Aghayev, Gylfi P Hersir, Jan Henninges, Michael Weber, and
559 Charlotte M Krawczyk. Dynamic strain determination using fibre-optic cables

- 560 allows imaging of seismological and structural features. *Nature communica-*
561 *tions*, 9(1):2509, 2018.
- [19] Chunquan Yu, Zhongwen Zhan, Nathaniel J Lindsey, Jonathan B Ajo-Franklin,
562 and Michelle Robertson. The potential of DAS in teleseismic studies: Insights
563 from the Goldstone experiment. *Geophysical Research Letters*, 46(3):1320–
564 1328, 2019.
- [20] Eileen R. Martin, Chris M Castillo, Steve Cole, Paphop Stock Sawasdee,
565 Siyuan Yuan, Robert Clapp, Martin Karrenbach, and Biondo L Biondi. Seismic
566 monitoring leveraging existing telecom infrastructure at the SDASA: Active,
567 passive, and ambient-noise analysis. *The Leading Edge*, 36(12):1025–1031,
568 2017.
- [21] M. Perton, F. J. Sánchez-Sesma, A. Rodríguez-Castellanos, M. Campillo, and
569 R. L. Weaver. Two perspectives on equipartition in diffuse elastic fields in
570 three dimensions. *The Journal of the Acoustical Society of America*, 126(3):
571 1125–1130, September 2009. ISSN 0001-4966. doi: 10.1121/1.3177262. URL
572 [http://scitation.aip.org/content/asa/journal/jasa/126/3/10.1121/1.](http://scitation.aip.org/content/asa/journal/jasa/126/3/10.1121/1.3177262)
573 [3177262.](http://scitation.aip.org/content/asa/journal/jasa/126/3/10.1121/1.3177262)
574 [1125–1130, September 2009. ISSN 0001-4966. doi: 10.1121/1.3177262. URL](http://scitation.aip.org/content/asa/journal/jasa/126/3/10.1121/1.3177262)
575 [http://scitation.aip.org/content/asa/journal/jasa/126/3/10.1121/1.](http://scitation.aip.org/content/asa/journal/jasa/126/3/10.1121/1.3177262)
576 [3177262.](http://scitation.aip.org/content/asa/journal/jasa/126/3/10.1121/1.3177262)
- [22] Zack J Spica, Mathieu Perton, Norimitsu Nakata, Xin Liu, and Gregory C
577 Beroza. Shallow v_s imaging of the Groningen area from joint inversion of
578 multi-mode surface waves and H/V spectral ratios. *Seismological Research*
579 *Letters*, 2018.
- [23] José Piña-Flores, Mathieu Perton, Antonio García-Jerez, Enrique Carmona,
580 Francisco Luzón, Juan C Molina-Villegas, and Francisco J Sánchez-Sesma.
581 The inversion of spectral ratio H/V in a layered system using the diffuse field
582 assumption (DFA). *Geophysical Journal International*, page ggw416, 2016.
- [24] Eileen R. Martin. *Passive imaging and characterization of the subsurface with*
583 *distributed acoustic sensing*. PhD thesis, Stanford University, June 2018.
- [25] P. Thomas, I. Wong, J. Zachariasen, R. Darragh, and W. Silva. 2013 update
584 to the sites-pecific seismic hazard analyses and development of seismic de-
585 sign ground motions: Stanford University, California. Technical report, Stan-
586 ford University, 2014.
- [26] Keith L Knudsen, Janet M Sowers, Robert C Witter, Carl M Wentworth, and
587 Edward J Helley. Description of mapping of quaternary deposits and liquefac-
588 tion susceptibility, nine-county San Francisco Bay Region, California. *Rep. No.*
589 *United States Geologic Survey Open-File Report 00*, 444, 2000.
- [27] Robert C Witter, Keith L Knudsen, Janet M Sowers, Carl M Wentworth,
590 Richard D Koehler, Carolyn E Randolph, Suzanna K Brooks, and Kathleen D
591

- 597 Gans. Maps of Quaternary deposits and liquefaction susceptibility in the cen-
598 tral San Francisco Bay region, California. Technical report, U.S. Geological
599 Survey, 2006.
- 600 [28] Robert Merton Hazlewood. Contour map and interpretive cross sections
601 showing depth and configuration of bedrock surface, south San Francisco Bay
602 region, California. Technical report, U.S. Geological Survey, 1976.
- 603 [29] Eileen R Martin, Nathaniel Lindsey, Jonathan Ajo-Franklin, and Biondo Biondi.
604 Introduction to interferometry of fiber optic strain measurements. 2018.
- 605 [30] ER Martin, BL Biondi, M Karrenbach, and S Cole. Continuous subsurface
606 monitoring by passive seismic with distributed acoustic sensors-the “Stanford
607 array” experiment. In *15th International Congress of the Brazilian Geophysi-
608 cal Society & EXPOGEF, Rio de Janeiro, Brazil, 31 July-3 August 2017*, pages
609 1366–1370. Brazilian Geophysical Society, 2017.
- 610 [31] USGS. U.S. Geological Survey Networks. International Federation of Digital
611 Seismograph Networks. Dataset/Seismic Network. doi: 10.7914/sn/gm. Tech-
612 nical report, 2016.
- 613 [32] Michel Bouchon. A review of the discrete wavenumber method. *Pure and
614 applied Geophysics*, 160(3-4):445–465, 2003.
- 615 [33] Xiangfang Zeng, Chelsea Lancelle, Clifford Thurber, Dante Fratta, Herb Wang,
616 Neal Lord, Athena Chalari, and Andy Clarke. Properties of noise cross-
617 correlation functions obtained from a distributed acoustic sensing array at
618 Garner Valley, California. *Bulletin of the Seismological Society of America*,
619 107(2):603–610, 2017.
- 620 [34] Ariel Lellouch, Si-yuan Tuan, Zack Spica, Biondo Biondi, and William
621 Ellsworth. Seismic velocity estimation using passive downhole distributed
622 acoustic sensing records - examples from the San Andreas Fault Observatory
623 at Depth. *Journal of Geophysical Research (Solid Earth)*, 2019.
- 624 [35] Hiroshi Arai and Kohji Tokimatsu. S-wave velocity profiling by inversion of
625 microtremor H/V spectrum. *Bulletin of the Seismological Society of America*,
626 94(1):53–63, February 2004. doi: 10.1785/0120030028.
- 627 [36] N. M. Shapiro and M. Campillo. Emergence of broadband Rayleigh waves
628 from correlations of the ambient seismic noise. *Geophysical Research Letters*,
629 31(7), 2004. ISSN 1944-8007. doi: 10.1029/2004GL019491.
- 630 [37] Charles A Langston. Structure under Mount Rainier, Washington, inferred
631 from teleseismic body waves. *Journal of Geophysical Research: Solid Earth*,
632 84(B9):4749–4762, 1979.

- 633 [38] Mathieu Perton, Marcial A Contreras-Zazueta, and Francisco J Sánchez-
 634 Sesma. Indirect boundary element method to simulate elastic wave propaga-
 635 tion in piecewise irregular and flat regions. *Geophysical Journal International*,
 636 205(3):1832–1842, 2016.
- 637 [39] G. D. Bensen, M. H. Ritzwoller, M. P. Barmin, A. L. Levshin, F. Lin, M. P.
 638 Moschetti, N. M. Shapiro, and Y. Yang. Processing seismic ambient noise
 639 data to obtain reliable broad-band surface wave dispersion measurements.
 640 *Geophysical Journal International*, 169(3):1239–1260, 2007. ISSN 1365-246X.
 641 doi: 10.1111/j.1365-246X.2007.03374.x.
- 642 [40] Antonio García-Jerez, José Piña-Flores, Francisco J. Sánchez-Sesma, Fran-
 643 cisco Luzón, and Mathieu Perton. A computer code for forward calcula-
 644 tion and inversion of the H/V spectral ratio under the diffuse field assump-
 645 tion. *Computers & Geosciences*, 97:67 – 78, 2016. ISSN 0098-3004. doi:
 646 10.1016/j.cageo.2016.06.016.
- 647 [41] Zack J Spica, Mathieu Perton, Nori Nakata, Xin Liu, and Gregory C Beroza.
 648 Site characterization at Groningen gas field area through joint surface-
 649 borehole H/V analysis. *Geophysical Journal International*, 212(1):412–421,
 650 2017. doi: 10.1093/gji/ggx426.
- 651 [42] Daniel E McNamara and Raymond P Buland. Ambient noise levels in the
 652 continental United States. *Bulletin of the seismological society of America*, 94
 653 (4):1517–1527, 2004.
- 654 [43] Jon Peterson et al. Observations and modeling of seismic background noise.
 655 *U.S. Geol. Surv. Open-File Rept.*, pages 95–322, 1993.